

Floquet higher-order topological phases in momentum space

Longwen Zhou^{1,*}

¹*Department of Physics, College of Information Science and Engineering,
Ocean University of China, Qingdao 266100, China*

(Dated: 2020-12-03)

Higher-order topological phases (HOTPs) are characterized by symmetry-protected bound states at the corners or hinges of the system. In this work, we reveal a momentum-space counterpart of HOTPs in time-periodic driven systems, which are demonstrated in a two-dimensional extension of the quantum double-kicked rotor. The found Floquet HOTPs are protected by chiral symmetry and characterized by a pair of topological invariants, which could take arbitrarily large integer values with the increase of kicking strengths. These topological numbers can also be measured from the chiral dynamics of wave packets. Under open boundary conditions, multiple quartets Floquet corner modes with zero and π quasienergies emerge in the system and coexist with delocalized bulk states at the same quasienergies, forming second-order Floquet topological bound states in continuum. The numbers of these corner modes are further counted by the bulk topological invariants according to the relation of bulk-corner correspondence. Our findings thus extend the study HOTPs to momentum-space lattices, and further uncover the richness of HOTPs and corner-localized bound states in continuum in Floquet driven systems.

I. INTRODUCTION

Higher-order topological phases (HOTPs) in D spatial dimensions are characterized by symmetry-protected states localized along its $(D-n)$ -dimensional boundaries, where $1 < n \leq D$ [1–8]. The existence of these unique topological matter is usually guaranteed by the coexistence of crystal and non-spatial symmetries, and their classifications go beyond the tenfold way of first-order topological insulators and superconductors [9–12]. Besides great theoretical efforts in the study of higher-order topological insulators [13–32], superconductors [33–48] and semimetals [49–54], HOTPs have also been observed in solid state materials [55–59], photonic waveguides [60–67], acoustic systems [68–75], electrical circuits [76–80] and superconducting qubits [81], leading to potential applications such as acoustic sensing [68, 69] and holonomic quantum computation [48].

In recent years, the study of HOTPs has been generalized to nonequilibrium systems, such as those subject to time-periodic drivings [82–94] or non-Hermitian effects [95–103]. The motivation behind the exploration of HOTPs in periodically driven systems is threefold. First, driving fields could induce symmetries and phase transitions that are unique to Floquet systems, yielding Floquet HOTPs with topological properties that go beyond any static counterparts [82, 93]. Second, periodic driving fields could in general enlarge the range of hoppings in a lattice, creating Floquet HOTPs with large topological numbers and many topological corner/hinge modes [82], which have potential applications in the construction of topological time crystals and Floquet quantum computing schemes [83]. Third, under appropriate conditions, certain Floquet systems could form lattice

structures in momentum space, whose topological properties are of intrinsic dynamical origins. Intriguing phenomena related to such momentum space topology including the quantized acceleration as an analogue of the Thouless pump [104], and the integer quantum Hall effects from chaos [105]. The first two aspects have led to the discoveries of a series of Floquet HOTPs in both Hermitian and non-Hermitian systems [82–95]. However, the momentum-space counterpart of Floquet HOTPs and their topological characterizations have rarely been explored.

In this manuscript, we investigate a periodically kicked particle in two spatial dimensions, whose momentum space could form a two-dimensional (2D) discrete lattice holding rich Floquet HOTPs. In Sec. II, we introduce the Hamiltonian of the system and obtain its Floquet operator under the quantum resonance condition. Based on the symmetry analysis of the model, we construct a pair of integer topological invariants (w_0, w_π) in Sec. III, which could fully characterize the Floquet HOTPs that are protected by the chiral symmetry of the system. These Floquet HOTPs are further shown to be able to possess arbitrary large topological numbers with the increase of kicking strengths. In Sec. IV, we show that these topological invariants could be dynamically probed by measuring the time-averaged mean chiral displacements (MCDs) of wave packets in two-dimension. Under the open boundary conditions (OBCs), we find many quartets of Floquet corner modes at zero and π quasienergies in Sec. V. The numbers of these corner modes are predicted by the bulk topological invariants (w_0, w_π) , yielding the bulk-corner correspondence of Floquet HOTPs in momentum space. Moreover, the zero and π Floquet corner modes are found to be embedded in the continuous bulk bands of delocalized states, forming corner-localized Floquet bound states in the continuum (BICs) that are originated from higher-order Floquet topology. We summarize our results and discuss

* zhoulw13@u.nus.edu

potential future directions in Sec. VI.

II. MODEL

In this section, we introduce a representative driven lattice model, which could possess rich Floquet HOTPs in momentum space. Our system can be viewed as a two-dimensional extension of the double kicked rotor (or lattice) model [106–109], which describes a quantum particle kicked twice by a periodic potential at different times within each driving period. The time-dependent Hamiltonian of the system takes the form

$$\hat{H} = \hat{H}_0 + \hat{V} \sum_{\ell \in \mathbb{Z}} \delta\left(\frac{t}{T} - \ell\right) + \hat{W} \sum_{\ell \in \mathbb{Z}} \delta\left(\frac{t - \tau}{T} - \ell\right), \quad (1)$$

where

$$\hat{H}_0 = \frac{\hat{p}_x^2 + \hat{p}_y^2}{2}, \quad (2)$$

$$\hat{V} = \kappa_1 \cos(\hat{x} + \phi_x) + \kappa_3 \cos(\hat{y} + \phi_y), \quad (3)$$

and

$$\hat{W} = \kappa_2 \cos(\hat{x}) + \kappa_4 \cos(\hat{y}). \quad (4)$$

Here (\hat{x}, \hat{y}) and (\hat{p}_x, \hat{p}_y) are the position and momentum operators of the particle along x and y directions. T is the driving period. $\tau \in (0, T)$ controls the time delay between the two kicks inside a driving period. $\kappa_{1,3}$ and $\kappa_{2,4}$ are kicking strengths of the potentials along x and y directions. $\phi_{x,y} \in [0, 2\pi)$ describe the phase differences between the kicking potentials applied at $t = \ell T$ and $t = \ell T + \tau$ in the ℓ 's driving period. The quantities in Eqs. (2)-(4) are all set in dimensionless units. In experiments, the model Hamiltonian \hat{H} may be realized in cold atom systems, where the kicking potentials could be implemented by optical-lattice potentials with relative phase shifts [108, 109]. Within a given driving period (e.g., from $t = 0^-$ to $t = T + 0^-$), the dynamics of the system is therefore governed by a kick \hat{V} applied at $t = 0$, followed by the free evolution \hat{H}_0 from $t = 0 \rightarrow \tau$, a second kick \hat{W} at $t = \tau$, and finally the free evolution \hat{H}_0 over a time duration $T - \tau$. The Floquet operator, which describes the evolution of the system over such a complete driving period, is then given by

$$\hat{U} = e^{-i\frac{T-\tau}{\hbar}\hat{H}_0} e^{-i\frac{\tau}{\hbar}\hat{W}} e^{-i\frac{\tau}{\hbar}\hat{H}_0} e^{-i\frac{\tau}{\hbar}\hat{V}}. \quad (5)$$

Due to the periodicity of kicking potentials \hat{V} and \hat{W} in \hat{x} and \hat{y} , the eigenvalues of momentum operators $\hat{p}_{x,y}$ take the forms $\hbar(n_{x,y} + k_{x,y})$, where $n_{x,y} \in \mathbb{Z}$, and $k_{x,y} \in [0, 1)$ are the quasimomenta. A Floquet system with periodicity in momentum space is achieved by setting $k_{x,y} = 0$, which may be realized experimentally by a Bose-Einstein

condensate with large coherence width [110–113]. Under this condition, we can identify the momentum operators $\hat{p}_{x,y}$ in Eq. (2) as $\hbar\hat{n}_{x,y}$ with integer eigenvalues $n_{x,y}$. The Floquet operator in Eq. (5) then takes the explicit form

$$\begin{aligned} \hat{U} &= e^{-i\hbar(T-\tau)\frac{\hat{n}_x^2 + \hat{n}_y^2}{2}} e^{-i[K_2 \cos(\hat{x}) + K_4 \cos(\hat{y})]} \\ &\times e^{-i\hbar\tau\frac{\hat{n}_x^2 + \hat{n}_y^2}{2}} e^{-i[K_1 \cos(\hat{x} + \phi_x) + K_3 \cos(\hat{y} + \phi_y)]}, \end{aligned} \quad (6)$$

where we have introduced $K_j = \kappa_j T / \hbar$ as rescaled dimensionless kicking strengths. Furthermore, under the quantum resonance condition $\hbar T = 4\pi$ that has been considered experimentally [110–116], we obtain the two-dimensional extension of on-resonance double kicked rotor (or lattice) model, whose Floquet operator reads

$$\begin{aligned} \hat{U} &= e^{i\hbar\tau\frac{\hat{n}_x^2 + \hat{n}_y^2}{2}} e^{-i[K_2 \cos(\hat{x}) + K_4 \cos(\hat{y})]} \\ &\times e^{-i\hbar\tau\frac{\hat{n}_x^2 + \hat{n}_y^2}{2}} e^{-i[K_1 \cos(\hat{x} + \phi_x) + K_3 \cos(\hat{y} + \phi_y)]}. \end{aligned} \quad (7)$$

It is then clear that once $\hbar\tau = 2\pi p/q$, with p and q being coprime integers, the Floquet operator \hat{U} will have translational symmetries in both \hat{n}_x and \hat{n}_y with the common period q , i.e., a periodic crystal structure in the momentum space of the two-dimensional on-resonance double-kicked lattice (2D-ORDKL). In one-dimensional (1D) descendant models of Eq. (7), rich first-order Floquet topological phases have been discovered, which are characterized by large Chern (winding numbers), multiple chiral (dispersionless) edge modes and topologically quantized acceleration in momentum space [104, 117–120]. These discoveries further motivate us to explore HOTPs in the 2D-ORDKL model.

To obtain a minimal version of the 2D-ORDKL with nontrivial higher-order topology, we choose the time delay between the two kicks to be $\tau = T/4$, which implies that $\hbar\tau = \pi$. Moreover, fixing the phase differences at $\phi_x = \phi_y = \pi/2$, the Floquet operator of the 2D-ORDKL reduces to

$$\begin{aligned} \hat{U} &= e^{i\frac{\pi}{2}(\hat{n}_x^2 + \hat{n}_y^2)} e^{-i[K_2 \cos(\hat{x}) + K_4 \cos(\hat{y})]} \\ &\times e^{-i\frac{\pi}{2}(\hat{n}_x^2 + \hat{n}_y^2)} e^{i[K_1 \sin(\hat{x}) + K_3 \sin(\hat{y})]}. \end{aligned} \quad (8)$$

Since $[\hat{n}_x, \hat{y}] = [\hat{n}_y, \hat{x}] = 0$, the 2D-ORDKL can be viewed as two 1D ORDKL models lying along two different spatial dimensions, i.e., $\hat{U} = \hat{U}_x \otimes \hat{U}_y$, where

$$\hat{U}_x = e^{i\frac{\pi}{2}\hat{n}_x^2} e^{-iK_2 \cos(\hat{x})} e^{-i\frac{\pi}{2}\hat{n}_x^2} e^{iK_1 \sin(\hat{x})}, \quad (9)$$

$$\hat{U}_y = e^{i\frac{\pi}{2}\hat{n}_y^2} e^{-iK_4 \cos(\hat{y})} e^{-i\frac{\pi}{2}\hat{n}_y^2} e^{iK_3 \sin(\hat{y})}. \quad (10)$$

By solving the Floquet eigenvalue equations $\hat{U}_x|\psi_x\rangle = e^{-iE_x}|\psi_x\rangle$ and $\hat{U}_y|\psi_y\rangle = e^{-iE_y}|\psi_y\rangle$, we could obtain the eigenstates $|\psi\rangle = |\psi_x\rangle \otimes |\psi_y\rangle$ of \hat{U} with eigenphases (quasienergies) $E = (E_x + E_y) \bmod 2\pi$. This observation immediately allows us to deduce the possible origin

of higher-order topology in the 2D-ORDKL. That is, if $|\psi_x\rangle$ and $|\psi_y\rangle$ are edge modes of \hat{U}_x and \hat{U}_y with eigenphases $(E_x, E_y) = (0, 0)$ or $(E_x, E_y) = (\pi, \pi)$, they will be coupled to form a corner mode of \hat{U} with eigenphase $E = E_x + E_y = 0$, i.e., a Floquet zero corner mode. Similarly, if $|\psi_x\rangle$ and $|\psi_y\rangle$ are edge modes of \hat{U}_x and \hat{U}_y with eigenphases $(E_x, E_y) = (0, \pi)$ or $(E_x, E_y) = (\pi, 0)$, they will be coupled to form a corner mode of \hat{U} with eigenphase $E = E_x + E_y = \pi$, i.e., a Floquet π corner mode. These are the two types of topological corner modes that could appear in Floquet HOTPs of the 2D-ORDKL, and their numbers are determined by the numbers of edge modes in the subsystems described by \hat{U}_x and \hat{U}_y , which are further determined by the winding numbers of \hat{U}_x and \hat{U}_y according to the principle of bulk-edge correspondence [121, 122]. In the following section, we will construct the bulk topological invariants for Floquet HOTPs in the 2D-ORDKL based on these analysis, and establish the topological phase diagram of the system.

III. TOPOLOGICAL INVARIANTS AND PHASE DIAGRAM

Since the Floquet operator \hat{U} in Eq. (8) possesses a tensor product structure, its spectrum and eigenstates are known once the eigenvalue equations $\hat{U}_j|\psi_j\rangle = e^{-iE_j}|\psi_j\rangle$ for $j = x, y$ are solved. Inserting the identity operators $\mathbb{I}_j = \sum_j |n_j\rangle\langle n_j|$ in the momentum space, and performing Fourier transforms from the momentum to quasiposition (the conserved quantity due to the translational symmetry $n_j \rightarrow n_j + 2$ in the momentum lattice) representation, the Floquet operator \hat{U}_j can be expressed in the form of

$$\hat{U}_j = \sum_{\theta_j} |\theta_j\rangle U_j(\theta_j) \langle \theta_j|, \quad (11)$$

where $\{|\theta_j\rangle\}$ is the eigenbasis of quasiposition with $\theta_j \in [0, 2\pi)$, and $j = x, y$. Explicitly, the Floquet matrices $U_x(\theta_x)$ and $U_y(\theta_y)$ are given by

$$U_x(\theta_x) = e^{i\frac{\pi}{4}\sigma_z} e^{-i\mathcal{K}_2(\cos\frac{\theta_x}{2}\sigma_x + \sin\frac{\theta_x}{2}\sigma_y)} \times e^{-i\frac{\pi}{4}\sigma_z} e^{i\mathcal{K}_1(\cos\frac{\theta_x}{2}\sigma_x + \sin\frac{\theta_x}{2}\sigma_y)}, \quad (12)$$

$$U_y(\theta_y) = e^{i\frac{\pi}{4}\tau_z} e^{-i\mathcal{K}_4(\cos\frac{\theta_y}{2}\tau_x + \sin\frac{\theta_y}{2}\tau_y)} \times e^{-i\frac{\pi}{4}\tau_z} e^{i\mathcal{K}_3(\cos\frac{\theta_y}{2}\tau_x + \sin\frac{\theta_y}{2}\tau_y)}, \quad (13)$$

with shorthand notations

$$\mathcal{K}_1 \equiv K_1 \sin\frac{\theta_x}{2}, \quad \mathcal{K}_2 \equiv K_2 \cos\frac{\theta_x}{2}, \quad (14)$$

$$\mathcal{K}_3 \equiv K_3 \sin\frac{\theta_y}{2}, \quad \mathcal{K}_4 \equiv K_4 \cos\frac{\theta_y}{2}. \quad (15)$$

Here $\sigma_{x,y,z}$ and $\tau_{x,y,z}$ denote Pauli matrices acting on two sublattice degrees of freedom along the x and y directions in the momentum lattice (see Refs. [118, 119] for derivation details of $U_j(\theta_j)$ for 1D descendant models of the 2D-ORDKL). The standard characterization of 1D Floquet topological phases is achieved by introducing a pair of symmetric time frames upon similarity transformations [121, 122]. For our 2D-ORDKL, there are two symmetric time frames for both $U_x(\theta_x)$ and $U_y(\theta_y)$. Putting together, there are in total four such time frames for the Floquet matrix $U(\theta_x, \theta_y) = U_x(\theta_x) \otimes U_y(\theta_y)$ of the 2D system. In these time frames, $U(\theta_x, \theta_y)$ takes the form

$$U_{\alpha\beta}(\theta_x, \theta_y) = U_\alpha(\theta_x) \otimes U_\beta(\theta_y), \quad (16)$$

where $\alpha = 1, 2, \beta = 3, 4$, and

$$U_1(\theta_x) = FG, \quad U_2(\theta_x) = GF, \quad (17)$$

$$U_3(\theta_y) = F'G', \quad U_4(\theta_y) = G'F'. \quad (18)$$

The auxiliary matrices F, G, F' and G' are explicitly given by (see Refs. [118, 119] for derivation details of these matrices for 1D descendant models of the 2D-ORDKL)

$$F \equiv e^{i\frac{\mathcal{K}_1}{2}(\cos\frac{\theta_x}{2}\sigma_x + \sin\frac{\theta_x}{2}\sigma_y)} e^{i\frac{\pi}{4}\sigma_z} e^{-i\frac{\mathcal{K}_2}{2}(\cos\frac{\theta_x}{2}\sigma_x + \sin\frac{\theta_x}{2}\sigma_y)}, \quad (19)$$

$$G \equiv e^{-i\frac{\mathcal{K}_2}{2}(\cos\frac{\theta_x}{2}\sigma_x + \sin\frac{\theta_x}{2}\sigma_y)} e^{-i\frac{\pi}{4}\sigma_z} e^{i\frac{\mathcal{K}_1}{2}(\cos\frac{\theta_x}{2}\sigma_x + \sin\frac{\theta_x}{2}\sigma_y)}, \quad (20)$$

$$F' \equiv e^{i\frac{\mathcal{K}_3}{2}(\cos\frac{\theta_y}{2}\tau_x + \sin\frac{\theta_y}{2}\tau_y)} e^{i\frac{\pi}{4}\tau_z} e^{-i\frac{\mathcal{K}_4}{2}(\cos\frac{\theta_y}{2}\tau_x + \sin\frac{\theta_y}{2}\tau_y)}, \quad (21)$$

$$G' \equiv e^{-i\frac{\mathcal{K}_4}{2}(\cos\frac{\theta_y}{2}\tau_x + \sin\frac{\theta_y}{2}\tau_y)} e^{-i\frac{\pi}{4}\tau_z} e^{i\frac{\mathcal{K}_3}{2}(\cos\frac{\theta_y}{2}\tau_x + \sin\frac{\theta_y}{2}\tau_y)}. \quad (22)$$

With these considerations, it is straightforward to verify that $U_{\alpha\beta}(\theta_x, \theta_y)$ possesses the chiral symmetry $\Gamma = \sigma_z \otimes \tau_z$ for all $\alpha = 1, 2$ and $\beta = 3, 4$, in the sense that

$$\Gamma U_{\alpha\beta}(\theta_x, \theta_y) \Gamma = U_{\alpha\beta}^\dagger(\theta_x, \theta_y). \quad (23)$$

This symmetry then allows us to characterize the Floquet HOTPs of the 2D-ORDKL by integer topological invariants [118, 121, 122].

To construct these topological numbers for our system, we take the Taylor expansion for each term of the Floquet matrices in Eqs. (17) and (18), and recombine the relevant terms. The resulting Floquet matrices take the forms

$$U_\alpha(\theta_x) = e^{-iE_x(\theta_x)[n_{\alpha x}(\theta_x)\sigma_x + n_{\alpha y}(\theta_x)\sigma_y]}, \quad (24)$$

$$U_\beta(\theta_y) = e^{-iE_y(\theta_y)[n_{\beta x}(\theta_y)\tau_x + n_{\beta y}(\theta_y)\tau_y]}, \quad (25)$$

where $\alpha = 1, 2$ and $\beta = 3, 4$. The eigenphase dispersions $E_x(\theta_x)$ and $E_y(\theta_y)$ along the two different dimensions are given by

$$E_x(\theta_x) = \arccos(\cos \mathcal{K}_1 \cos \mathcal{K}_2), \quad (26)$$

$$E_y(\theta_y) = \arccos(\cos \mathcal{K}_3 \cos \mathcal{K}_4). \quad (27)$$

The explicit expressions of unit vectors $[n_{\alpha x}(\theta_x), n_{\alpha y}(\theta_x)]$ and $[n_{\beta x}(\theta_y), n_{\beta y}(\theta_y)]$ are summarized in the Appendix A. In the quasiposition representation, the 2D-ORDKL model then possesses four eigenphase (quasienergy) bands, whose dispersion relations are given by

$$E_{ss'}(\theta_x, \theta_y) = sE_x(\theta_x) + s'E_y(\theta_y), \quad (28)$$

where $s, s' = \pm$. The system could undergo topological phase transitions when these bands touch and separate at the quasienergies zero and π .

In previous studies [118, 119], it has been demonstrated that a 1D system described by the Floquet operator $U_\alpha(\theta_x)$ or $U_\beta(\theta_y)$ possesses a topological winding number

$$w_\nu = \int_0^{2\pi} \frac{d\theta_j}{2\pi} \partial_{\theta_j} \varphi_\nu(\theta_j), \quad (29)$$

where $\nu = \{\alpha, \beta\}$, $j = x, y$, and the winding angle $\varphi_\nu(\theta_j)$ in the ν 's time frame is defined as

$$\varphi_\nu(\theta_j) \equiv \arctan[n_{\nu y}(\theta_j)/n_{\nu x}(\theta_j)]. \quad (30)$$

Using these winding numbers, we can further construct two pairs of invariants $(w_{0x}, w_{\pi x})$ and $(w_{0y}, w_{\pi y})$ for the Floquet subsystems described by \hat{U}_x and \hat{U}_y , respectively [121, 122]. They are related to the values of w_ν through the relations

$$w_{0x} = \frac{w_1 + w_2}{2}, \quad w_{\pi x} = \frac{w_1 - w_2}{2}, \quad (31)$$

$$w_{0y} = \frac{w_3 + w_4}{2}, \quad w_{\pi y} = \frac{w_3 - w_4}{2}. \quad (32)$$

These invariants always take integer quantized values. They provide a complete characterization of the topological phases in 1D Floquet systems with chiral (sublattice) symmetry [121, 122]. Moreover, under the open boundary condition, the invariants w_{0x} (w_{0y}) and $w_{\pi x}$ ($w_{\pi y}$) could predict the numbers of topological edge modes with quasienergies zero and π in the subsystem described by \hat{U}_x (\hat{U}_y) [118, 119], and therefore also capturing the bulk-edge correspondence of these Floquet subsystems.

For our 2D-ORDKL model, the Floquet HOTPs can be characterized by appropriate combinations of these 1D topological numbers. Specially, referring to our analysis on how the zero and π Floquet edge modes can be coupled to form corner modes in the last section, we introduce a pair of topological invariants (w_0, w_π) for the

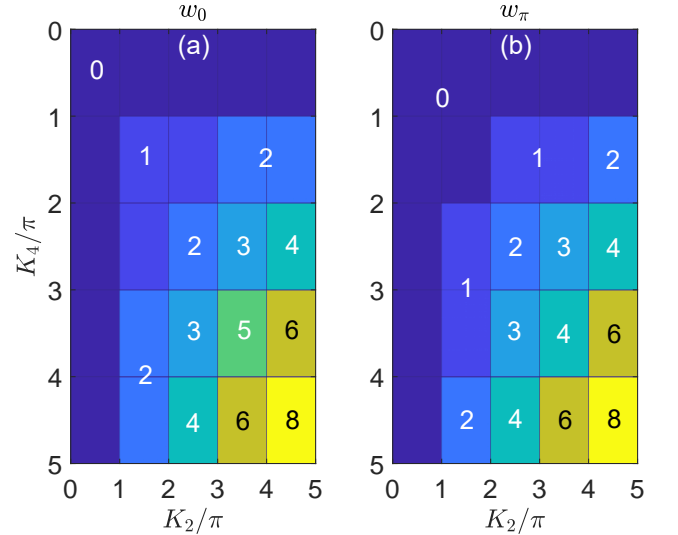


FIG. 1. Topological phase diagram of the 2D-ORDKL versus the kicking strengths K_2 and K_4 . The other system parameters are set as $K_1 = K_3 = 0.5\pi$. Different Floquet HOTPs are distinguished by different colors in each figure panel. The values of w_0 (w_π) for different topological phases are obtained from Eq. (33) [(34)] and denoted explicitly in panel (a) [(b)].

2D-ORDKL, which are defined as

$$w_0 \equiv |w_{0x}w_{0y}| + |w_{\pi x}w_{\pi y}|, \quad (33)$$

$$w_\pi \equiv |w_{0x}w_{\pi y}| + |w_{\pi x}w_{0y}|. \quad (34)$$

It is clear that $(w_0, w_\pi) \in \mathbb{Z} \times \mathbb{Z}$ due to the quantized nature of w_{0j} and $w_{\pi j}$ ($j = x, y$). Furthermore, as will be demonstrated in Sec. V, the values of w_0 and w_π could correctly count the numbers of Floquet corner modes with quasienergies zero and π in the momentum space of the 2D-ORDKL. Therefore, the invariants (w_0, w_π) could provide us with a complete characterization of Floquet HOTPs in the 2D-ORDKL, and other chiral symmetric 2D lattice models with Floquet operators in the form of $\hat{U} = \hat{U}_x \otimes \hat{U}_y$. We also notice that $(w_0, w_\pi) \neq (0, 0)$ only when the subsystems described by \hat{U}_x and \hat{U}_y are both topologically nontrivial. The Floquet HOTPs of the 2D-ORDKL are thus originated from the cooperation of topological natures of the two subsystems in lower dimensions.

In the remaining part of this section, based on the evaluation of invariants w_0 and w_π in Eqs. (33) and (34), we present topological phase diagrams of the 2D-ORDKL for two typical situations. In the first case, we show the phase diagram of the system with respect to the kicking strengths (K_2, K_4) in Fig. 1. We observe that with the increase of these kicking strengths, a series of topological phase transitions can be induced, which each of them being accompanied by the quantized jump of w_0 or w_π . At large values of (K_2, K_4) , we further obtain rich Floquet HOTPs characterized by large values of (w_0, w_π) .

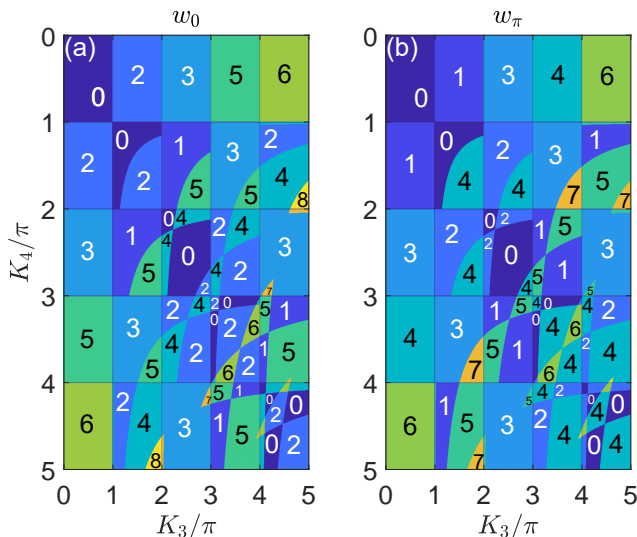


FIG. 2. Topological phase diagram of the 2D-ORDKL with respect to the kicking strengths K_3 and K_4 . The other system parameters are set as $(K_1, K_2) = (0.5\pi, 3.5\pi)$. Different Floquet HOTPs are distinguished by different colors in both figure panels. The values of w_0 and w_π for each topological phase are obtained from Eqs. (33) and (34), which are presented explicitly in figure panels (a) and (b), respectively.

It is not hard to verify that there is no upper bound for the values of these invariants if the kicking strengths keep increasing. Therefore, the 2D-ORDKL serves as a good candidate to generate Floquet HOTPs in momentum space with arbitrarily large topological invariants. Besides, according to the tensor product structure of Floquet operator in Eq. (16), the boundaries separating different Floquet HOTPs are determined by the gapless conditions along one dimension of the lattice. More explicitly, these phase boundaries are determined by the conditions $\cos[E_x(\theta_x)] = \pm 1$ and $\cos[E_y(\theta_y)] = \pm 1$, or equivalently

$$\frac{m_1^2}{K_1^2} + \frac{m_2^2}{K_2^2} = \frac{1}{\pi^2}, \quad \frac{m_3^2}{K_3^2} + \frac{m_4^2}{K_4^2} = \frac{1}{\pi^2}, \quad (35)$$

with $m_i \in \mathbb{Z}$ and $|m_i\pi/K_i| \leq 1$ for $i = 1, 2, 3, 4$. In Fig. 1, our choice of system parameters yield $m_1 = m_3 = 0$, and the phase boundaries are reduced to straight lines according to Eq. (35), which is also consistent with the numerical results.

In the second case, we present the phase diagram of the 2D-ORDKL versus kicking strengths (K_3, K_4) in Fig. 2. With the increase of these kicking strengths, we also observe rich Floquet HOTPs featured by large invariants (w_0, w_π) , together with multiple transitions between these phases followed by quantized changes of (w_0, w_π) . Numerically, we have also checked the phase diagrams of the system versus any one pair of kicking parameters $(K_i, K_{i'})$, with the other pair being fixed for $i, i' = 1, 2, 3, 4$, and obtain similar patterns for the topo-

logical phases and phase transitions. Therefore, we conclude that the 2D-ORDKL indeed possesses rich Floquet HOTPs, which are characterized by a pair integer topological invariants (w_0, w_π) . These invariants could not only predict the numbers of Floquet zero and π corner modes in the system under OBCs, but also be detectable experimentally from the dynamics of wavepackets, as will be presented in the following sections.

IV. MEAN CHIRAL DISPLACEMENTS

In this section, we sketch a dynamical approach that can be used to probe the invariants (w_0, w_π) of Floquet HOTPs in the 2D-ORDKL. This approach is based on the detection of a 2D extension of the time-averaged mean chiral displacement (MCD), which was introduced in Refs. [82, 95]. In a 2D lattice (either in position or momentum space), we define the chiral displacement operator of the dynamical evolution in the time frame (α, β) as

$$\hat{C}_{\alpha\beta}(t) = \hat{U}_{\alpha\beta}^{-t}(\hat{N}_x \otimes \Gamma_x) \otimes (\hat{N}_y \otimes \Gamma_y) \hat{U}_{\alpha\beta}^t. \quad (36)$$

Here t counts the number of evolution periods. The Floquet operator $\hat{U}_{\alpha\beta} = \hat{U}_\alpha \otimes \hat{U}_\beta$, as defined in Eq. (16) for $\alpha = 1, 2$ and $\beta = 3, 4$. \hat{N}_x and \hat{N}_y are unit-cell position operators along x and y directions of the lattice. Γ_x and Γ_y describe chiral symmetries of the descendant systems \hat{U}_α and \hat{U}_β along x and y directions, respectively. For the 2D-ORDKL model, we have $\Gamma_x = \sigma_z$ and $\Gamma_y = \tau_z$, whose tensor product gives the chiral symmetry operator Γ of the 2D system.

To extract the topological winding numbers of $\hat{U}_{\alpha\beta}$, we initialize the system in a fully polarized state at the central unit cell of the lattice. The initial state vector then takes the form

$$|\psi_0\rangle = |0_x\rangle \otimes |\uparrow_x\rangle \otimes |0_y\rangle \otimes |\uparrow_y\rangle, \quad (37)$$

where $|0_x\rangle$ ($|0_y\rangle$) is the eigenstate of \hat{N}_x (\hat{N}_y) with eigenvalue $N_x = 0$ ($N_y = 0$). $|\uparrow_x\rangle$ and $|\uparrow_y\rangle$ are the eigenvectors of Γ_x and Γ_y with eigenvalues $+1$. After the evolution over a number of t 's driving periods in the time frame (α, β) , the MCD of initial state $|\psi_0\rangle$ is given by the expectation value

$$C_{\alpha\beta}(t) = \langle \psi_0 | \hat{C}_{\alpha\beta}(t) | \psi_0 \rangle. \quad (38)$$

Since $|\psi_0\rangle$ is not an eigenstate of $\hat{U}_{\alpha\beta}$, $C_{\alpha\beta}(t)$ is expected to be an oscillating function of time. To extract the topological information from $C_{\alpha\beta}(t)$, we take the average $\bar{C}_{\alpha\beta}(t)$ over many driving periods, which in the long-time limit yields the stroboscopic time-averaged MCD

$$\bar{C}_{\alpha\beta} = \lim_{t \rightarrow \infty} \frac{1}{t} \sum_{t'=1}^t C_{\alpha\beta}(t'). \quad (39)$$

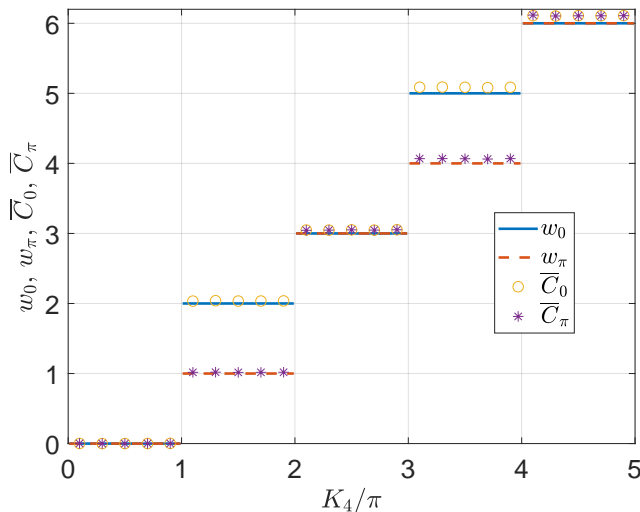


FIG. 3. Topological invariants (w_0, w_π) and time-averaged MCDs $(\overline{C}_0, \overline{C}_\pi)$ of the 2D-ORDKL versus the kicking strength K_4 . The other system parameters are set as $K_1 = 0.5\pi$, $K_2 = 3.5\pi$ and $K_3 = 0.5\pi$. The MCDs are averaged over $t = 50$ driving periods to generate the results for $(\overline{C}_0, \overline{C}_\pi)$.

Following the derivation steps as detailed in Ref. [82], it can be shown that for $\alpha = 1, 2$ and $\beta = 3, 4$,

$$\overline{C}_{\alpha\beta} = \frac{w_\alpha w_\beta}{4}. \quad (40)$$

Here w_α and w_β are the winding numbers defined in Eq. (29). With the help of Eqs. (31) and (32), we can recombine the time-averaged MCDs to obtain the products of winding numbers $w_{0x}w_{0y}$, $w_{0x}w_{\pi y}$, $w_{\pi x}w_{0y}$ and $w_{\pi x}w_{\pi y}$, which finally yield the invariants (w_0, w_π) of the Floquet HOTPs. From now on, we will denote the recombined time-averaged MCDs that are related to w_0 and w_π as \overline{C}_0 and \overline{C}_π , respectively (see Appendix B for their explicit expressions).

To verify the relations between the time-averaged MCDs and the topological invariants of the 2D-ORDKL, we compute and compare (w_0, w_π) and $(\overline{C}_0, \overline{C}_\pi)$ for a typical case in the remaining part of this section. In Fig. 3, we present the topological invariants and MCDs with respect to the kicking strength K_4 for evolutions over $t = 50$ driving periods. We observe that the time-averaged MCDs $(\overline{C}_0, \overline{C}_\pi)$ indeed take nearly quantized values in each Floquet HOTPs of the 2D-ORDKL, which demonstrate the relation between them and the topological invariants of the system, i.e., $(\overline{C}_0, \overline{C}_\pi) = (w_0, w_\pi)$ (see Appendix B for derivation details of this relation). Besides, the values of $(\overline{C}_0, \overline{C}_\pi)$ also possess quantized jumps around all topological phase transition points ($K_4 = \pi, 2\pi, 3\pi, 4\pi$ in Fig. 3). Therefore, the MCDs could also serve as a dynamical prob to the phase transitions between different Floquet HOTPs. The deviations of $(\overline{C}_0, \overline{C}_\pi)$ from quantization is due to finite-time effects, which will gradually go to zero with the increase of the number of driving periods t . Numerically, we have

checked that the time-averaged MCDs $(\overline{C}_0, \overline{C}_\pi)$ remain close to quantization for $t = 20$ driving periods, which should be within reach in current or near-term experiments in photonic [123, 124] and cold atom [125, 126] systems.

In the following section, we will demonstrate another topological signature of Floquet HOTPs, i.e., the symmetry protected bound states localized around the corners of the momentum-space lattice, and relate their numbers to the topological invariants (w_0, w_π) of the system.

V. FLOQUET TOPOLOGICAL CORNER BOUND STATES IN CONTINUUM

A defining feature of the HOTP in D spatial dimensions are symmetry-protected states localized along its $(D - d)$ -dimensional boundaries, where $d > 1$. For a 2D lattice studied in this work, such bound states could appear at the geometric corners of the system. Moreover, since the Floquet bands of a chiral symmetric system come in positive and negative pairs $\pm E$, they could touch and separate at the quasienergies zero and π . Therefore, in principle there could be two distinct types of Floquet corner modes appearing at these quasienergies, which will be called Floquet zero and π corner modes. In the 2D-ORDKL described by $\hat{U} = \hat{U}_x \otimes \hat{U}_y$, since these corner modes are formed by the coupling between doubly degenerate edge modes of 1D descendant systems \hat{U}_x and \hat{U}_y , their numbers (N_0, N_π) are always integer multiples of four. Furthermore, the numbers (N_0, N_π) of Floquet zero and π corner modes tend out to be connected with the bulk topological invariants (w_0, w_π) of the 2D-ORDKL through the relation

$$(N_0, N_\pi) = 4(w_0, w_\pi). \quad (41)$$

The Eq. (41) thus establishes the bulk-corner correspondence of Floquet HOTPs in the 2D-ORDKL and other chiral symmetric systems, whose Floquet operators can be expressed in the tensor product form of $\hat{U} = \hat{U}_x \otimes \hat{U}_y$. The implication of Eq. (41) will be demonstrated in the following with explicit numerical examples.

To investigate the spectrum and states of the system under OBCs, we express the operators in Eqs. (9) and (10) in momentum representations as

$$\hat{U}_x = e^{i\frac{\pi}{2} \sum_{n_x} n_x^2 |n_x\rangle \langle n_x|} e^{-i\frac{K_2}{2} \sum_{n_x} (|n_x\rangle \langle n_x+1| + \text{h.c.})} \times e^{-i\frac{\pi}{2} \sum_{n_x} n_x^2 |n_x\rangle \langle n_x|} e^{i\frac{K_1}{2i} \sum_{n_x} (|n_x\rangle \langle n_x+1| - \text{h.c.})}, \quad (42)$$

$$\hat{U}_y = e^{i\frac{\pi}{2} \sum_{n_y} n_y^2 |n_y\rangle \langle n_y|} e^{-i\frac{K_4}{2} \sum_{n_y} (|n_y\rangle \langle n_y+1| + \text{h.c.})} \times e^{-i\frac{\pi}{2} \sum_{n_y} n_y^2 |n_y\rangle \langle n_y|} e^{i\frac{K_3}{2i} \sum_{n_y} (|n_y\rangle \langle n_y+1| - \text{h.c.})}. \quad (43)$$

The quasienergies E and Floquet eigenstates $|\psi\rangle$ of the system are then obtained by solving the eigenvalue equation $\hat{U}|\psi\rangle = e^{-iE}|\psi\rangle$, where the diagonalization of \hat{U} can

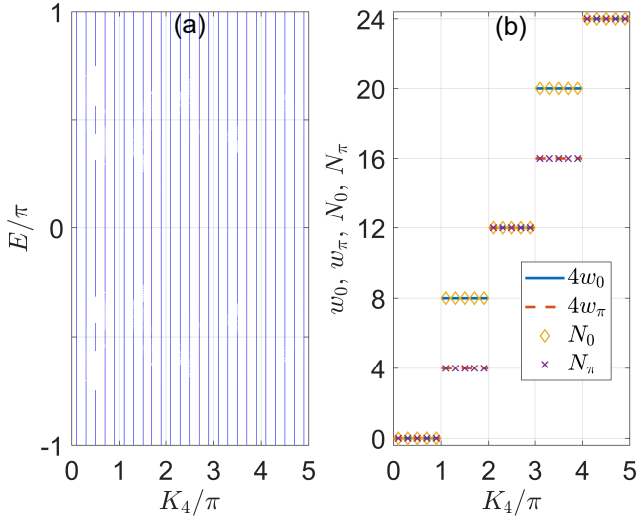


FIG. 4. Floquet spectrum E and number of corner modes (N_0, N_π) of the 2D-ORDKL versus the kicking strength K_4 . The other system parameters are set as $(K_1, K_2, K_3) = (0.5\pi, 3.5\pi, 0.5\pi)$. The size of the lattice is $L_x = L_y = 300$. In panel (b), N_0 and N_π are plotted together with the bulk topological invariants w_0 and w_π as obtained from Eqs. (33) and (34).

be performed separately for \hat{U}_x and \hat{U}_y due to the tensor product structure of the Floquet operator $\hat{U} = \hat{U}_x \otimes \hat{U}_y$.

In Fig. 4, we present the quasienergy spectrum E and number of Floquet corner modes N_0 and N_π at zero and π quasienergies in the momentum space of 2D-ORDKL. In Fig. 4(a), we observe an almost continuous Floquet spectrum with no gaps around the quasienergies $E = 0$ and $E = \pi$. This is different from the situations usually observed in 2D static and Floquet HOTPs, where corner modes are separated from bulk states by spectral gaps. However, by evaluating the inverse partition ratio (IPR)

$$\text{IPR} \equiv \sum_{n_x, n_y} |\psi(n_x, n_y)|^4 \quad (44)$$

for all the Floquet eigenstates of \hat{U} , we find different numbers of corner modes N_0 and N_π at the quasienergies zero and π in distinct Floquet HOTPs of the system. Their numbers are presented together with the topological invariants w_0 and w_π in Fig. 4(b). Note that the IPRs of corner modes are different from bulk and 1D edge states of the system in their order of magnitudes, and can thus be numerically distinguished from one another. Furthermore, we observe that the relation $(N_0, N_\pi) = 4(w_0, w_\pi)$ holds throughout the considered parameter regime, validating the bulk-corner correspondence of the 2D-ORDKL as established in Eq. (41). Besides, with the increase of K_4 , the system undergoes a series of topological phase transitions, yielding Floquet HOTPs with more and more zero and π corner modes. The 2D-ORDKL thus provides us with a nice platform to investigate Floquet HOTPs with multiple corner states and strong topological sig-

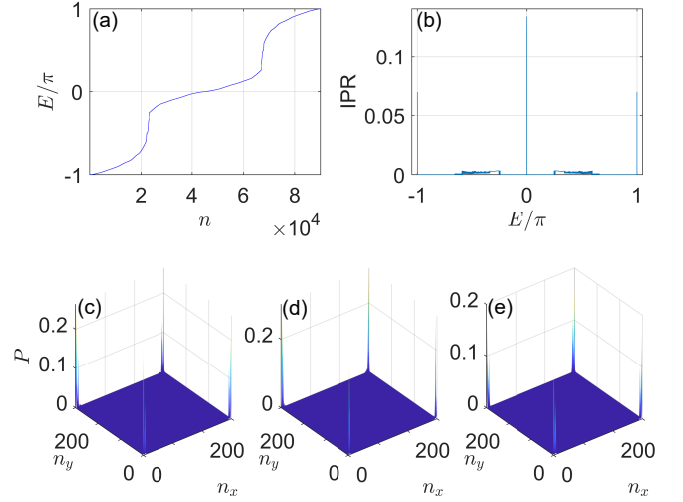


FIG. 5. Quasienergy spectrum, IPR and Floquet zero/ π corner modes of the 2D-ORDKL. System parameters are set as $K_1 = 0.5\pi$, $K_2 = 3.5\pi$, $K_3 = 0.5\pi$ and $K_4 = 1.5\pi$. The size of the lattice is $L_x = L_y = 300$. In panel (a), n denotes the index of the state. The peaks around $E = \pm\pi$ ($E = 0$) in panel (b) correspond to the IPRs of π (zero) Floquet corner modes, whose probability distributions are shown in panel (c) [(d) and (e)].

natures. For completeness, we have also checked the quasienergy spectrum and corner modes in other parameter regions of the system, and obtain results that are consistent with the above descriptions.

In Fig. 5, we present the quasienergy spectrum, IPR and corner modes of the system for a typical situation. In Fig. 5(a), we observe that the Floquet spectrum E spread throughout the first quasienergy Brillouin zone, and no gaps can be observed around $E = 0, \pm\pi$. However, in Fig. 5(b), we find three clear peaks in the IPR versus the quasienergy E around $E = 0$ and $E = \pm\pi$, which indicates the existence of localized bound states in the system at these quasienergies. By investigating the data, we obtain eight (four) such bound states at $E = 0$ ($E = \pm\pi$), with their probability distributions shown explicitly in Figs. 5(d,e) [Fig. 5(f)]. We see that all of these bound states are indeed localized around the corners of the system, and their numbers are determined precisely by the bulk-corner correspondence relation in Eq. (41) for the given set of system parameters. Therefore, these corner states originate from the higher-order topology of the 2D-ORDKL. They represent topologically degenerate corner modes in momentum space of the system, which are protected by the chiral symmetry Γ . Besides, these corner modes coexist with extended bulk states at the same quasienergies. We therefore refer to them as corner-localized Floquet topological bound states in continuum, in the sense that they do not hybridize with the surrounding bulk states even without a bulk band gap. This observation also extends the scope of bulk-corner correspondence of Floquet HOTPs to more general situations, in which the symmetry-protected corner modes

can not only be found in spectral gaps, but also appear within topological Floquet bands. Note in passing that the corner-localized BICs with zero energy have been discovered before in static HOTPs [127–129]. By contrast, the corner-localized Floquet BICs subject to different topological characterizations, and the corner BICs with quasienergy $E = \pi$ are unique to Floquet HOTPs found in this work. Experimentally, the implementation of OBCs in momentum space might be a challenging task. However, by applying the mapping introduced in Ref. [118] from momentum to position space lattices, the 2D-ORDKL may also be realized in real space, and the corner modes may then be probed in setups like photonic waveguide arrays [129].

VI. CONCLUSION

In this work, we find rich Floquet HOTPs in a 2D extension of the on-resonance double kicked rotor. Each of the Floquet HOTP is characterized by a pair of integer topological invariants (w_0, w_π) , which can be extracted from the dynamics of the system in four distinct symmetric time frames. The values of w_0 and w_π take quantized jumps whenever the system undergoes a transition between different Floquet HOTPs. Furthermore, Floquet HOTPs characterized by arbitrarily large (w_0, w_π) can be found in principle with the increase of kicking strengths. Experimentally, the invariants (w_0, w_π) could also be obtained by measuring the time-averaged mean chiral displacements of initially localized wavepackets in different time frames. Under open boundary conditions, corner-localized modes with quasienergies zero and π are found to be coexisting with extended bulk states at the same quasienergies, realizing second-order Floquet topological bound states in continuum. The numbers of these corner modes are further determined by the bulk topological invariants (w_0, w_π) , leading to the bulk-corner correspondence of Floquet HOTPs. Even though the direct detection of these corner modes in momentum space could be challenging due to the implementation of OBCs, the double kicked rotor could be mapped to a periodically quenched tight-binding lattice [118]. Therefore, our model may also be engineered in two-dimensional photonic or cold atom systems, where the Floquet corner modes could be imaged in real-space. Putting together, we uncovered a unique set of Floquet HOTPs in momentum space, which are featured by large topological invariants and multiple topological corner bound states in continuum. In future studies, it would be interesting to extend our results to Floquet HOTPs in higher dimensions, exploring the possibilities of realizing topological time crystals by superposing these zero and π Floquet corner modes, and investigating the potential applications of these corner bound states in Floquet quantum computing tasks.

ACKNOWLEDGEMENT

L.Z. acknowledges Yuhong Zhu for helpful discussions. This work is supported by the National Natural Science Foundation of China (Grant No. 11905211), the China Postdoctoral Science Foundation (Grant No. 2019M662444), the Fundamental Research Funds for the Central Universities (Grant No. 841912009), the Young Talents Project at Ocean University of China (Grant No. 861801013196), and the Applied Research Project of Postdoctoral Fellows in Qingdao (Grant No. 861905040009).

Appendix A: Components of the effective Hamiltonian

In this appendix, we summarize the explicit expressions of unit vectors $[n_{\alpha x}(\theta_x), n_{\alpha y}(\theta_x)]$ and $[n_{\beta x}(\theta_y), n_{\beta y}(\theta_y)]$ for $\alpha = 1, 2$ and $\beta = 3, 4$ in Eqs. (24) and (25) of the main text, respectively. Following the derivation steps as sketched in the main text and detailed in Refs. [118, 119] for 1D descendant models of the 2D-ORDKL, the components of these unit vectors are found to be

$$n_{1x}(\theta_x) = -\frac{\cos \frac{\theta_x}{2} \sin \mathcal{K}_1 \cos \mathcal{K}_2 - \sin \frac{\theta_x}{2} \sin \mathcal{K}_2}{\sin[E_x(\theta_x)]}, \quad (\text{A1})$$

$$n_{1y}(\theta_x) = -\frac{\sin \frac{\theta_x}{2} \sin \mathcal{K}_1 \cos \mathcal{K}_2 + \cos \frac{\theta_x}{2} \sin \mathcal{K}_2}{\sin[E_x(\theta_x)]}, \quad (\text{A2})$$

$$n_{2x}(\theta_x) = +\frac{\cos \frac{\theta_x}{2} \cos \mathcal{K}_1 \sin \mathcal{K}_2 + \sin \frac{\theta_x}{2} \sin \mathcal{K}_1}{\sin[E_x(\theta_x)]}, \quad (\text{A3})$$

$$n_{2y}(\theta_x) = +\frac{\sin \frac{\theta_x}{2} \cos \mathcal{K}_1 \sin \mathcal{K}_2 - \cos \frac{\theta_x}{2} \sin \mathcal{K}_1}{\sin[E_x(\theta_x)]}, \quad (\text{A4})$$

and

$$n_{3x}(\theta_y) = -\frac{\cos \frac{\theta_y}{2} \sin \mathcal{K}_3 \cos \mathcal{K}_4 - \sin \frac{\theta_y}{2} \sin \mathcal{K}_4}{\sin[E_y(\theta_y)]}, \quad (\text{A5})$$

$$n_{3y}(\theta_y) = -\frac{\sin \frac{\theta_y}{2} \sin \mathcal{K}_3 \cos \mathcal{K}_4 + \cos \frac{\theta_y}{2} \sin \mathcal{K}_4}{\sin[E_y(\theta_y)]}, \quad (\text{A6})$$

$$n_{4x}(\theta_y) = +\frac{\cos \frac{\theta_y}{2} \cos \mathcal{K}_3 \sin \mathcal{K}_4 + \sin \frac{\theta_y}{2} \sin \mathcal{K}_3}{\sin[E_y(\theta_y)]}, \quad (\text{A7})$$

$$n_{4y}(\theta_y) = +\frac{\sin \frac{\theta_y}{2} \cos \mathcal{K}_3 \sin \mathcal{K}_4 - \cos \frac{\theta_y}{2} \sin \mathcal{K}_3}{\sin[E_y(\theta_y)]}. \quad (\text{A8})$$

Here $\mathcal{K}_{1,2}$ and $\mathcal{K}_{3,4}$ are given by Eqs. (14) and (15) of the main text, respectively.

Appendix B: Relation between MCDs and topological invariants

In this appendix, we present the explicit relationship between the time-averaged MCDs and the topological invariants of the 2D-ORDKL model. Following Eqs. (31), (32) and (40) in the main text, it is straightforward to verify the following equalities between the time-averaged MCDs and winding numbers in different combinations of symmetric frames

$$\overline{C}_{13} + \overline{C}_{14} + \overline{C}_{23} + \overline{C}_{24} = w_{0x}w_{0y}, \quad (\text{B1})$$

$$\overline{C}_{13} - \overline{C}_{14} - \overline{C}_{23} + \overline{C}_{24} = w_{\pi x}w_{\pi y}, \quad (\text{B2})$$

$$\overline{C}_{13} - \overline{C}_{14} + \overline{C}_{23} - \overline{C}_{24} = w_{0x}w_{\pi y}, \quad (\text{B3})$$

$$\overline{C}_{13} + \overline{C}_{14} - \overline{C}_{23} - \overline{C}_{24} = w_{\pi x}w_{0y}. \quad (\text{B4})$$

Combining these equations with the definitions of w_0 and w_π in Eqs. (33) and (34) of the main text, we find

$$\begin{aligned} \overline{C}_0 &\equiv |\overline{C}_{13} + \overline{C}_{14} + \overline{C}_{23} + \overline{C}_{24}| \\ &+ |\overline{C}_{13} - \overline{C}_{14} - \overline{C}_{23} + \overline{C}_{24}| = w_0, \end{aligned} \quad (\text{B5})$$

$$\begin{aligned} \overline{C}_\pi &\equiv |\overline{C}_{13} - \overline{C}_{14} + \overline{C}_{23} - \overline{C}_{24}| \\ &+ |\overline{C}_{13} + \overline{C}_{14} - \overline{C}_{23} - \overline{C}_{24}| = w_\pi. \end{aligned} \quad (\text{B6})$$

Therefore, by measuring the time-averaged MCDs $\overline{C}_{\alpha\beta}$ for $\alpha = 1, 2$ and $\beta = 3, 4$, we could obtain the invariants (w_0, w_π) of Floquet HOTPs from wavepacket dynamics in different time frames.

-
- [1] W. A. Benalcazar, B. A. Bernevig, and T. L. Hughes, *Science* **357**, 61 (2017).
- [2] W. A. Benalcazar, B. A. Bernevig, and T. L. Hughes, *Phys. Rev. B* **96**, 245115 (2017).
- [3] Z. Song, Z. Fang, and C. Fang, *Phys. Rev. Lett.* **119**, 246402 (2017).
- [4] J. Langbehn, Y. Peng, L. Trifunovic, F. von Oppen, and P. W. Brouwer, *Phys. Rev. Lett.* **119**, 246401 (2017).
- [5] K. Hashimoto, X. Wu, and T. Kimura, *Phys. Rev. B* **95**, 165443 (2017).
- [6] F. Schindler, A. M. Cook, M. G. Vergniory, Z. Wang, S. S. P. Parkin, B. A. Bernevig, and T. Neupert, *Sci. Adv.* **4**, eaat0346 (2018).
- [7] F. Liu and K. Wakabayashi, *Phys. Rev. Lett.* **118**, 076803 (2017).
- [8] R.-J. Slager, L. Rademaker, J. Zaanen, and L. Balents, *Phys. Rev. B* **92**, 085126 (2015).
- [9] E. Khalaf, H. C. Po, A. Vishwanath, and H. Watanabe, *Phys. Rev. X* **8**, 031070 (2018).
- [10] E. Cornfeld and A. Chapman, *Phys. Rev. B* **99**, 075105 (2019).
- [11] L. Trifunovic and P. W. Brouwer, *Phys. Status Solidi B* **2020**, 2000090.
- [12] J. Kruthoff, J. de Boer, J. van Wezel, C. L. Kane, and R.-J. Slager, *Phys. Rev. X* **7**, 041069 (2017).
- [13] S. Franca, J. van den Brink, and I. C. Fulga, *Phys. Rev. B* **98**, 201114(R) (2018).
- [14] M. Ezawa, *Phys. Rev. Lett.* **121**, 116801 (2018).
- [15] E. Khalaf, *Phys. Rev. B* **97**, 205136 (2018).
- [16] F. Liu, H.-Y. Deng, and K. Wakabayashi, *Phys. Rev. Lett.* **122**, 086804 (2019).
- [17] L. Trifunovic and P. W. Brouwer, *Phys. Rev. X* **9**, 011012 (2019).
- [18] F. K. Kunst, G. van Miert, and E. J. Bergholtz, *Phys. Rev. B* **97**, 241405(R) (2018).
- [19] K. Kudo, T. Yoshida, and Y. Hatsugai, *Phys. Rev. Lett.* **123**, 196402 (2019).
- [20] T. I. Tügel, V. Chua, and T. L. Hughes, *Phys. Rev. B* **100**, 115126 (2019).
- [21] F. Zangeneh-Nejad and R. Fleury, *Phys. Rev. Lett.* **123**, 053902 (2019).
- [22] O. Pozo, C. Repellin, and A. G. Grushin, *Phys. Rev. Lett.* **123**, 247401 (2019).
- [23] M. J. Park, Y. Kim, G. Y. Cho, and S. Lee, *Phys. Rev. Lett.* **123**, 216803 (2019).
- [24] Y. Hwang, J. Ahn, and B.-J. Yang, *Phys. Rev. B* **100**, 205126 (2019).
- [25] H. Araki, *Phys. Rev. Res.* **2**, 012009(R) (2020).
- [26] L. Li, M. Umer, and J. Gong, *Phys. Rev. B* **98**, 205422 (2018).
- [27] R. Chen, C.-Z. Chen, J.-H. Gao, B. Zhou, and D.-H. Xu, *Phys. Rev. Lett.* **124**, 036803 (2020).
- [28] H. Li and K. Sun, *Phys. Rev. Lett.* **124**, 036401 (2020).
- [29] Y. Xu, Z. Song, Z. Wang, H. Weng, and X. Dai, *Phys. Rev. Lett.* **122**, 256402 (2019).
- [30] R. Queiroz and A. Stern, *Phys. Rev. Lett.* **123**, 036802 (2019).
- [31] R. Kozlovsky, A. Graf, D. Kochan, K. Richter, and C. Gorini, *Phys. Rev. Lett.* **124**, 126804 (2020).
- [32] R. Queiroz, I. C. Fulga, N. Avraham, H. Beidenkopf, and J. Cano, *Phys. Rev. Lett.* **123**, 266802 (2019).
- [33] Z. Yan, *Phys. Rev. Lett.* **123**, 177001 (2019).
- [34] Z. Yan, F. Song, and Z. Wang, *Phys. Rev. Lett.* **121**, 096803 (2018).
- [35] R.-X. Zhang, W. S. Cole, X. Wu, and S. Das Sarma, *Phys. Rev. Lett.* **123**, 167001 (2019).
- [36] C. Zeng, T. D. Stanescu, C. Zhang, V. W. Scarola, and S. Tewari, *Phys. Rev. Lett.* **123**, 060402 (2019).
- [37] M. Geier, L. Trifunovic, M. Hoskam, and P. W. Brouwer, *Phys. Rev. B* **97**, 205135 (2018).
- [38] X. Zhu, *Phys. Rev. Lett.* **122**, 236401 (2019).
- [39] S. A. A. Ghorashi, X. Hu, T. L. Hughes, and E. Rossi, *Phys. Rev. B* **100**, 020509(R) (2019).
- [40] D. Varjas, A. Lau, K. Pöyhönen, A. R. Akhmerov, *Phys. Rev. Lett.* **123**, 196401 (2019).

- [41] S.-B. Zhang and B. Trauzettel, *Phys. Rev. Res.* **2**, 012018(R) (2020).
- [42] S. Franca, D. V. Efremov, and I. C. Fulga, *Phys. Rev. B* **100**, 075415 (2019).
- [43] Q. Wang, C.-C. Liu, Y.-M. Lu, and F. Zhang, *Phys. Rev. Lett.* **121**, 186801 (2018).
- [44] C.-H. Hsu, P. Stano, J. Klinovaja, and D. Loss, *Phys. Rev. Lett.* **121**, 196801 (2018).
- [45] Y. Volpez, D. Loss, and J. Klinovaja, *Phys. Rev. Lett.* **122**, 126402 (2019).
- [46] R.-X. Zhang, W. S. Cole, and S. Das Sarma, *Phys. Rev. Lett.* **122**, 187001 (2019).
- [47] X.-H. Pan, K.-J. Yang, L. Chen, G. Xu, C.-X. Liu, and X. Liu, *Phys. Rev. Lett.* **123**, 156801 (2019).
- [48] S.-B. Zhang, W. B. Rui, A. Calzona, S.-J. Choi, A. P. Schnyder, and B. Trauzettel, *Phys. Rev. Res.* **2**, 043025 (2020).
- [49] M. Lin and T. L. Hughes, *Phys. Rev. B* **98**, 241103(R) (2018).
- [50] D. Calugaru, V. Juricic, and B. Roy, *Phys. Rev. B* **99**, 041301(R) (2019).
- [51] B. Roy, *Phys. Rev. Res.* **1**, 032048(R) (2019).
- [52] M. Ezawa, *Phys. Rev. Lett.* **120**, 026801 (2018).
- [53] B. J. Wieder, Z. Wang, J. Cano, X. Dai, L. M. Schoop, B. Bradlyn, and B. A. Bernevig, *Nat. Commun.* **11**, 627 (2020).
- [54] Z. Wang, B. J. Wieder, J. Li, B. Yan, and B. A. Bernevig, *Phys. Rev. Lett.* **123**, 186401 (2019).
- [55] F. Schindler, Z. Wang, M. G. Vergniory, A. M. Cook, A. Murani, S. Sengupta, A. Yu. Kasumov, R. Deblock, S. Jeon, I. Drozdov, H. Bouchiat, S. Guéron, A. Yazdani, B. A. Bernevig, and T. Neupert, *Nat. Phys.* **14**, 918-924 (2018).
- [56] S. N. Kempkes, M. R. Slot, J. J. van den Broeke, P. Capiod, W. A. Benalcazar, D. Vanmaekelbergh, D. Bercioux, I. Swart, and C. Morais Smith, *Nature Materials* **18**, 1292-1297 (2019).
- [57] R.-X. Zhang, F. Wu, and S. Das Sarma, *Phys. Rev. Lett.* **124**, 136407 (2020).
- [58] Y. Yang, Z. Jia, Y. Wu, Z.-H. Hang, H. Jiang, and X. C. Xie, *Science Bulletin* **65**, 531 (2020).
- [59] X.-L. Sheng, C. Chen, H. Liu, Z. Chen, and Z.-M. Yu, *Phys. Rev. Lett.* **123**, 256402 (2019).
- [60] M. Serra-Garcia, V. Peri, R. Süssstrunk, O. R. Bilal, T. Larsen, L. G. Villanueva, and S. D. Huber, *Nature* **555**, 342-345 (2018).
- [61] C. W. Peterson, W. A. Benalcazar, T. L. Hughes, and G. Bahl, *Nature* **555**, 346-350 (2018).
- [62] S. Mittal, V. V. Orre, G. Zhu, M. A. Gorlach, A. Poddubny, and M. Hafezi, *Nature Photonics* **13**, 692-696 (2019).
- [63] A. E. Hassan, F. K. Kunst, A. Moritz, G. Andler, E. J. Bergholtz, and M. Bourennane, *Nature Photonics* **13**, 697-700 (2019).
- [64] X.-D. Chen, W.-M. Deng, F.-L. Shi, F.-L. Zhao, M. Chen, and J.-W. Dong, *Phys. Rev. Lett.* **122**, 233902 (2019).
- [65] B.-Y. Xie, G.-X. Su, H.-F. Wang, H. Su, X.-P. Shen, P. Zhan, M.-H. Lu, Z.-L. Wang, and Y.-F. Chen, *Phys. Rev. Lett.* **122**, 233903 (2019).
- [66] Y. Ota, F. Liu, R. Katsumi, K. Watanabe, K. Wakabayashi, Y. Arakawa, and S. Iwamoto, *Optica* **6**, 786-789 (2019).
- [67] Y. Wang, Y. Ke, Y.-J. Chang, Y.-H. Lu, J. Gao, C. Lee, and X.-M. Jin, arXiv:2011.11027.
- [68] H. Xue, Y. Yang, F. Gao, Y. Chong, and B. Zhang, *Nature Materials* **18**, 108-112 (2019).
- [69] X. Ni, M. Weiner, A. Alù, and A. B. Khanikaev, *Nature Materials* **18**, 113-120(2019).
- [70] V. Peri, Z.-D. Song, M. Serra-Garcia, P. Engeler, R. Queiroz, X. Huang, W. Deng, Z. Liu, B. A. Bernevig, and S. D. Huber, *Science* **367**, 797-800 (2020).
- [71] X. Zhang, H.-X. Wang, Z.-K. Lin, Y. Tian, B. Xie, M.-H. Lu, Y.-F. Chen, and J.-H. Jiang, *Nat. Phys.* **15**, 582-588 (2019).
- [72] M. Weiner, X. Ni, M. Li, A. Alù, and A. B. Khanikaev, *Sci. Adv.* **6**, eaay4166 (2020).
- [73] H. Fan, B. Xia, L. Tong, S. Zheng, and D. Yu, *Phys. Rev. Lett.* **122**, 204301 (2019).
- [74] H. Xue, Y. Yang, G. Liu, F. Gao, Y. Chong, and B. Zhang, *Phys. Rev. Lett.* **122**, 244301 (2019).
- [75] X. Zhang, Z.-K. Lin, H.-X. Wang, Z. Xiong, Y. Tian, M.-H. Lu, Y.-F. Chen, and J.-H. Jiang *Nat. Commun.* **11**, 65 (2020).
- [76] S. Imhof, C. Berger, F. Bayer, J. Brehm, L. W. Molenkamp, T. Kiessling, F. Schindler, C. H. Lee, M. Greiter, T. Neupert, and R. Thomale, *Nat. Phys.* **14**, 925-929 (2018).
- [77] M. Serra-Garcia, R. Süssstrunk, and S. D. Huber, *Phys. Rev. B* **99**, 020304(R) (2019).
- [78] J. Bao, D. Zou, W. Zhang, W. He, H. Sun, and X. Zhang, *Phys. Rev. B* **100**, 201406(R) (2019).
- [79] W. Zhang, D. Zou, W. He, J. Bao, Q. Pei, H. Sun, and X. Zhang, *Phys. Rev. B* **102**, 100102(R) (2020).
- [80] J. Wu, X. Huang, J. Lu, Y. Wu, W. Deng, F. Li, and Z. Liu, *Phys. Rev. B* **102**, 104109 (2020).
- [81] J. Niu, T. Yan, Y. Zhou, Z. Tao, X. Li, W. Liu, L. Zhang, S. Liu, Z. Yan, Y. Chen, and D. Yu, arXiv:2001.03933.
- [82] R. W. Bomantara, L. Zhou, J. Pan, and J. Gong, *Phys. Rev. B* **99**, 045441 (2019).
- [83] R. W. Bomantara and J. Gong, *Phys. Rev. B* **101**, 085401 (2020).
- [84] Y. Peng and G. Refael, *Phys. Rev. Lett.* **123**, 016806 (2019).
- [85] H. Hu, B. Huang, E. Zhao, and W. V. Liu, *Phys. Rev. Lett.* **124**, 057001 (2020).
- [86] T. Nag, V. Juricic, and B. Roy, *Phys. Rev. Res.* **1**, 032045(R) (2019).
- [87] M. Rodriguez-Vega, A. Kumar, and B. Seradjeh, *Phys. Rev. B* **100**, 085138 (2019).
- [88] R. Seshadri, A. Dutta, and D. Sen, *Phys. Rev. B* **100**, 115403 (2019).
- [89] K. Plekhanov, M. Thakurathi, D. Loss, and J. Klinovaja, *Phys. Rev. Res.* **1**, 032013(R) (2019).
- [90] Y. Peng, *Phys. Rev. Res.* **2**, 013124 (2020).
- [91] A. K. Ghosh, G. C. Paul, and A. Saha, *Phys. Rev. B* **101**, 235403 (2020).
- [92] R. W. Bomantara, *Phys. Rev. Res.* **2**, 033495 (2020).
- [93] R.-X. Zhang and Z.-C. Yang, arXiv:2010.07945.
- [94] W. Zhu, Y. D. Chong, and J. Gong, arXiv:2010.03879.
- [95] J. Pan and L. Zhou, *Phys. Rev. B* **102**, 094305 (2020).
- [96] T. Liu, Y.-R. Zhang, Q. Ai, Z. Gong, K. Kawabata, M. Ueda, and F. Nori, *Phys. Rev. Lett.* **122**, 076801 (2019).
- [97] Z. Zhang, M. R. López, Y. Cheng, X. Liu, and J. Christensen, *Phys. Rev. Lett.* **122**, 195501 (2019).

- [98] X.-W. Luo and C. Zhang, *Phys. Rev. Lett.* **123**, 073601 (2019).
- [99] C. H. Lee, L. Li, and J. Gong, *Phys. Rev. Lett.* **123**, 016805 (2019).
- [100] M. Ezawa, *Phys. Rev. B* **99**, 201411(R) (2019).
- [101] M. Ezawa, *Phys. Rev. B* **99**, 121411(R) (2019).
- [102] E. Edvardsson, F. K. Kunst, and E. J. Bergholtz, *Phys. Rev. B* **99**, 081302(R) (2019).
- [103] A. Yoshida, Y. Otaki, R. Otaki, and T. Fukui, *Phys. Rev. B* **100**, 125125 (2019).
- [104] D. Y. H. Ho and J. Gong, *Phys. Rev. Lett.* **109**, 010601 (2012).
- [105] Y. Chen and C. Tian, *Phys. Rev. Lett.* **113**, 216802 (2014).
- [106] J. Wang and J. B. Gong, *Phys. Rev. E* **78**, 036219 (2008).
- [107] J. Wang and J. B. Gong, *Phys. Rev. A* **77**, 031405 (2008).
- [108] P. H. Jones, M. M. Stocklin, G. Hur, and T. S. Monteiro, *Phys. Rev. Lett.* **93**, 223002 (2004).
- [109] C. E. Creffield, G. Hur, and T. S. Monteiro, *Phys. Rev. Lett.* **96**, 024103 (2006).
- [110] I. Dana, V. Ramareddy, I. Talukdar, and G. S. Summy, *Phys. Rev. Lett.* **100**, 024103 (2008).
- [111] M. Sadgrove, M. Horikoshi, T. Sekimura, and K. Nakagawa, *Phys. Rev. Lett.* **99**, 043002 (2007).
- [112] C. Ryu, M. F. Andersen, A. Vaziri, M. B. d'Arcy, J. M. Grossman, K. Helmerson, and W. D. Phillips, *Phys. Rev. Lett.* **96**, 160403 (2006).
- [113] I. Talukdar, R. Shrestha, and G. S. Summy, *Phys. Rev. Lett.* **105**, 054103 (2010).
- [114] F. L. Moore, J. C. Robinson, C. F. Bharucha, B. Sundaram, and M. G. Raizen, *Phys. Rev. Lett.* **75**, 4598 (1995).
- [115] J. F. Kanem, S. Maneshi, M. Partlow, M. Spanner, and A. M. Steinberg, *Phys. Rev. Lett.* **98**, 083004 (2007).
- [116] A. Ullah and M. D. Hoogerland, *Phys. Rev. E* **83**, 046218 (2011).
- [117] H. Wang, D. Y. H. Ho, W. Lawton, J. Wang, and J. Gong, *Phys. Rev. E* **88**, 052920 (2013).
- [118] D. Y. H. Ho and J. Gong, *Phys. Rev. B* **90**, 195419 (2014).
- [119] L. Zhou and J. Pan, *Phys. Rev. A* **100**, 053608 (2019).
- [120] L. Zhou and J. Gong, *Phys. Rev. A* **97**, 063603 (2018).
- [121] J. K. Asbóth, *Phys. Rev. B* **86**, 195414 (2012).
- [122] J. K. Asbóth and H. Obuse, *Phys. Rev. B* **88**, 121406(R) (2013).
- [123] F. Cardano, A. D'Errico, A. Dauphin, M. Maffei, B. Piccirillo, C. de Lisio, G. D. Filippis, V. Cataudella, E. Santamato, L. Marrucci, M. Lewenstein, and P. Massignan, *Nat. Commun.* **8**, 15516 (2017).
- [124] A. D'Errico, F. Di Colandrea, R. Barboza, A. Dauphin, M. Lewenstein, P. Massignan, L. Marrucci, and F. Cardano, *Phys. Rev. Res.* **2**, 023119 (2020).
- [125] E. J. Meier, F. A. An, A. Dauphin, M. Maffei, P. Massignan, T. L. Hughes, and B. Gadway, *Science* **362**, 929 (2018).
- [126] D. Xie, T.-S. Deng, T. Xiao, W. Gou, T. Chen, W. Yi, and B. Yan, *Phys. Rev. Lett.* **124**, 050502 (2020).
- [127] Z.-G. Chen, C. Xu, R. A. Jahdali, J. Mei, and Y. Wu, *Phys. Rev. B* **100**, 075120 (2019).
- [128] W. A. Benalcazar and A. Cerjan, *Phys. Rev. B* **101**, 161116(R) (2020).
- [129] A. Cerjan, M. Jürgensen, W. A. Benalcazar, S. Mukherjee, and M. C. Rechtsman, *Phys. Rev. Lett.* **125**, 213901 (2020).